

# Modeling Low Reynolds Number Incompressible Flows Using SPH

Joseph P. Morris, Patrick J. Fox, and Yi Zhu

*School of Civil Engineering, Purdue University, West Lafayette, Indiana 47907*

E-mail: jpmorris@ecn.purdue.edu

Received December 16, 1996; revised June 12, 1997

The method of smoothed particle hydrodynamics (SPH) is extended to model incompressible flows of low Reynolds number. For such flows, modification of the standard SPH formalism is required to minimize errors associated with the use of a quasi-incompressible equation of state. Treatment of viscosity, state equation, kernel interpolation, and boundary conditions are described. Simulations using the method show close agreement with series solutions for Couette and Poiseuille flows. Furthermore, comparison with finite element solutions for flow past a regular lattice of cylinders shows close agreement for the velocity and pressure fields. The SPH results exhibit small pressure fluctuations near curved boundaries. Further improvements to the boundary conditions may be possible which will reduce these errors. A similar method to that used here may permit the simulation of other flows at low Reynolds numbers using SPH. Further development will be needed for cases involving free surfaces or substantially different equations of state. © 1997 Academic Press

## 1. INTRODUCTION

The study of incompressible fluid flows in which viscous forces are either comparable with or dominate inertial forces has applications to many physical problems. Industrial, biological, and environmental processes often involve flows of low Reynolds number ( $Re$ ). Many applications to the fields of environmental, mechanical, chemical, and petroleum engineering likewise involve slow viscous incompressible flows through filters, substrates, porous materials, and other potentially deformable structures.

Smoothed particle hydrodynamics (SPH), while originally developed for astrophysical applications [1, 2], has been applied successfully to a wide range of problems. SPH is a fully Lagrangian technique in which the numerical solution is achieved without a grid. An advantage of SPH is the relative ease with which new physics may be incorporated into the formulation. It is also straightforward to allow boundaries to move or deform and to model the interaction of several fluid phases bounded by a free surface. SPH has certain advantages over other fluid dynamical methods, which may, for example, encounter difficulty with deformable boundaries, multiphase fluids, free surfaces, and the extension to three dimensions. While SPH is a versatile method, errors can sometimes be larger than

those obtained using grid-based methods tailored for specific problems. Moreover, SPH can be more computationally expensive than alternative techniques for a given application.

For typical astrophysical applications, SPH is used to model compressible fluids at high Reynolds number (usually  $Re \geq 10^3$  [4]). Although SPH has been used to model free surface flows of inviscid incompressible fluids [3], and some research has been performed using SPH for compressible gases with Reynolds numbers down to five [5], low Reynolds number ( $Re \leq 1$ ) incompressible flows have not been modeled using SPH. The objective of this paper is to present modifications of the standard SPH formalism needed to simulate such flows. Treatment of viscosity, equation of state, kernel interpolation, and boundary conditions are described. Simulations using the method show close agreement with series solutions for Couette and Poiseuille flows and with finite element solutions for flow past a regular lattice of cylinders.

## 2. THE METHOD

### 2.1. Background

Using SPH the fluid is represented by particles, typically of fixed mass, which follow the fluid motion, advect contact discontinuities, preserve Galilean invariance, and reduce computational diffusion of various fluid properties including momentum. The equations governing the evolution of the fluid become expressions for interparticle forces and fluxes when written in SPH form. Using the standard approach to SPH [6, 7], the particles (which may also be regarded as interpolation points) move with the local fluid velocity. Each particle carries mass  $m$ , velocity  $\mathbf{v}$ , and other fluid quantities specific to a given problem. The equations governing the evolution of fluid quantities are expressed as summation interpolants using a kernel function  $W$  with smoothing length  $h$ . For example, the density at particle  $a$ ,  $\rho_a$ , may be evaluated using

$$\rho_a = \sum_b m_b W_{ab}, \quad (1)$$

where  $W_{ab}$  denotes

$$W_{ab} = W(\mathbf{r}_{ab}, h) \quad (2)$$

and

$$\mathbf{r}_{ab} = \mathbf{r}_a - \mathbf{r}_b, \quad (3)$$

where  $\mathbf{r}_a$  denotes the position of particle  $a$ . The kernel typically takes the form

$$W(\mathbf{r}_{ab}, h) = \frac{1}{h^\sigma} f\left(\frac{|\mathbf{r}_{ab}|}{h}\right), \quad (4)$$

where  $\sigma$  is the number of dimensions and the function  $f$  is discussed in Section 2.7. Other expressions for quantities at the particles are obtained by summation involving the kernel or its derivatives. For example, the most common SPH expression for the pressure gradient term is

$$-\left(\frac{1}{\rho} \nabla p\right)_a = -\sum_b m_b \left(\frac{p_a}{\rho_a^2} + \frac{p_b}{\rho_b^2}\right) \nabla_a W_{ab}, \quad (5)$$

where  $p_a$  is the pressure at particle  $a$  and  $\nabla_a$  denotes the gradient with respect to the coordinates of particle  $a$ . For a kernel of the form in (4), this pressure gradient formulation conserves momentum exactly, since forces acting between individual particles are antisymmetric.

The following sections consider specific aspects of the SPH formalism and the approaches necessary to simulate incompressible flows at low Reynolds number.

## 2.2. Evolution of Density

If (1) is used when modeling incompressible free-surface flows, particle density is smoothed out at the edge of the fluid and spurious pressure gradients are induced at the surface. To avoid this problem, Monaghan [3] initially set the density to a reference value and evolved particle densities according to the following SPH equation for continuity:

$$\frac{d\rho_a}{dt} = \sum_b m_b \mathbf{v}_{ab} \cdot \nabla_a W_{ab}. \quad (6)$$

Our test cases do not involve free surfaces, and thus (1) may be used to evolve particle densities. One disadvantage of this approach is that  $\rho$  must be evaluated by summing over the particles before other quantities may be interpolated. However, (6) allows  $\rho$  to be evolved concurrently with particle velocities and other field quantities, thus significantly reducing the computational effort. While (6) does not conserve mass exactly ((1) does, provided the total number and mass of particles are constant), this is

usually only important for faster flows involving shocks. The simulations presented here, therefore, use (6) to evolve density.

## 2.3. Dynamic Pressure

For low Reynolds number flows, local variations in the pressure gradient which force the fluid motion can be very small, compared with the hydrostatic pressure gradient. This is of special significance to SPH, since pressure is obtained using an explicit function of density and is only accurate to about 1% (see the following section). For many problems it is simpler to use SPH to model the dynamic pressure,  $p_d$ , defined as

$$p_d = p_t - p_h, \quad (7)$$

where  $p_t$  and  $p_h$  are the total and hydrostatic pressures, respectively. Since pressure appears in the Navier–Stokes equations only as a gradient, the effect of  $p_h$  is that of a body force,

$$\begin{aligned} -\frac{1}{\rho} \nabla p_t &= -\frac{1}{\rho} \nabla p_d - \frac{1}{\rho} \nabla p_h, \\ &= -\frac{1}{\rho} \nabla p_d + \mathbf{F}, \end{aligned} \quad (8)$$

where  $\mathbf{F}$  is a force per unit mass. Using this approach, pressure gradient driven flow through a periodic lattice can be easily simulated (see Section 3.3). Periodic boundary conditions are applied to all fluid quantities and the flow is driven by the effective body force. The dynamic pressure is modeled using the equation of state (see (10) in Section 2.4). For simplicity,  $p$  is used in the following sections to denote the dynamic pressure  $p_d$ .

## 2.4. Equation of State

Most grid-based techniques model the flow of water as incompressible since the speed of sound in water is usually large compared with bulk fluid motions (i.e., a very low Mach number). Using SPH, fluid pressure is an explicit function of local fluid density and particle motions are driven by local density gradients. Therefore, it is necessary to use a quasi-incompressible equation of state to model such flows with SPH. Since the actual equation of state for water would require a prohibitively small time step for stability (by the CFL condition [8]), an artificial state equation is used. The chosen sound speed is low enough to be practical, yet high enough to limit density fluctuations to within 3%. A similar approach has been used in grid-based techniques to model steady incompressible flow [9–11]. Previous applications of SPH to incompressible flows

[3–12] have employed a state equation suggested by Batchelor [13],

$$p = p_0 \left\{ \left( \frac{\rho}{\rho_0} \right)^\gamma - 1 \right\}, \quad (9)$$

where  $\gamma = 7$  and a zero subscript denotes reference quantities. The choice of  $\gamma = 7$  in (9) causes pressure to respond strongly to variations in density. Thus, perturbations to the density field remain small, even at high Reynolds numbers. However, as the density fluctuations increase, small errors in density correspond to increasingly larger errors in pressure. For lower Reynolds numbers, more accurate pressure estimates are obtained using SPH if  $\gamma$  is taken to be unity (as it is in [9–11]), since errors in density and pressure remain proportional.

In previous work involving incompressible fluids, the subtraction of 1 in (9) was introduced to remove spurious boundary effects at a free surface. It is well established that SPH is unstable when attractive forces act between particles [14–17, 29]. Consequently, for the simulations presented in Section 3, this subtraction was found to lead to numerical instabilities in regions of sustained low pressure. Since the test simulations (and many applications) have particles filling all space, this work uses

$$p = c^2 \rho, \quad (10)$$

where  $c$  is the speed of sound.

The sound speed must be chosen carefully to ensure both an efficient and accurate solution of a given problem. The value of  $c$  must be large enough that the behavior of the corresponding quasi-incompressible fluid is sufficiently close to that of the real fluid, yet it should not be so large as to make the time step prohibitively small. Using a scale analysis, Monaghan [3] argued that, for density to vary by at most 1%, the Mach number of the flow should be 0.1 or less. In fact, for typical smoothing lengths used with SPH, kernel interpolation is only accurate to within approximately 1%. The principal cause of this variation is small fluctuations in density which inevitably occur as particles move past one another. Thus, pressure gradients obtained using a high sound speed are potentially noisy. Nevertheless, the velocities obtained are accurate if smoothed either by XSPH [18] or viscosity. For many applications, a close estimate of bulk fluid motion is sufficient. However, for other problems, accurate estimates of the pressure field are needed. We found that computed pressures are in close agreement with other techniques when  $c$  is chosen such that the density varies by at most 3%.

It is possible to estimate an appropriate value of  $c$  by considering the balance of forces in the Navier–Stokes momentum equation,

$$\frac{d\mathbf{v}}{dt} = -\frac{1}{\rho} \nabla p + \nu \nabla^2 \mathbf{v} + \mathbf{F}, \quad (11)$$

where  $\nu$  is the kinematic viscosity and  $\mathbf{F}$  is a body force per unit mass. Substituting a velocity scale  $V_0$ , a length scale  $L_0$ , and a body force per unit mass of magnitude  $F$  into (11), we find that the square of the sound speed should be comparable with the largest of

$$c^2 \sim \frac{V_0^2}{\delta}, \frac{\nu V_0}{L_0 \delta}, \frac{FL_0}{\delta}, \quad (12)$$

where

$$\delta = \frac{\Delta \rho}{\rho_0}. \quad (13)$$

The first term in (12) corresponds to that derived by Monaghan [3]. The second and third terms ensure that pressure forces are comparable with viscous and body forces, respectively. These conditions should only be regarded as a guide to an estimate of an appropriate sound speed. After a simulation has been run initially at low resolution and the actual variation in  $p$  is known, the value of  $c$  can be changed to produce the desired density variation.

## 2.5. Boundary Conditions

Initial applications of quasi-incompressible SPH involved high Reynolds number simulations of free surface flows interacting with free-slip boundaries. Such work employed boundary particles which exerted strong repulsive forces to prevent SPH particles from penetrating solid surfaces [3, 19, 20]. To realistically model flows at lower Reynolds numbers, no-slip boundary conditions are needed. In addition, for the free surface flows considered by Monaghan [3], boundary particles do not contribute to the density of the free SPH particles, thus permitting the fluid to freely leave a solid boundary with no pressure-driven restoring force. For our work, boundary particles contribute to the density of fluid particles such that pressure decreases when fluid and boundary particles diverge. It is possible to implement such a boundary condition using image particles [21]. These images are created by reflecting fluid particles across the boundary with opposite velocities. This procedure works well for straight channels, but introduces density errors for curved surfaces. Takeda *et al.* [5] achieved a no-slip boundary condition using special boundary terms which mimic a half-space filled with SPH image particles. While these approaches have proved useful for compressible and moderate to high Reynolds number flows, we found they did not give sufficiently stable results for our simulations.

In this work, actual SPH particles are used to represent a no-slip boundary surface. These particles contribute to the usual SPH expressions for density and pressure gradients, and their own densities are also evolved. Evolving the densities of boundary particles was found to better capture peak pressures than if boundary densities were kept constant. Obstacles within the flow are created by placing all the particles on a regular lattice throughout the computational domain and designating those particles falling within a solid object to be boundary particles. The advantage of this approach is that a “quiet” start is guaranteed since the particle number density is initially constant throughout the computational domain. However, it can lead to an imperfect representation of a curved boundary at low resolution. An alternative would be to place boundary particles on the surface of each obstacle. One difficulty with this method is “filling” the fluid space with a distribution of free particles corresponding to constant density. In this case, the initial configuration can be “relaxed” to a quiet state before driving forces are applied. The former approach was used in this work for simplicity.

A first-order no-slip condition can be created if boundary particles are moved with the velocity of the object to which they are attached. However, this approach can produce significant errors in velocity near boundaries. Antisymmetry can be approximated by extrapolating the velocity of free particles through the boundary to the position of the boundary particles. Ideally, a local estimate of the velocity gradients at the surface of the boundary would be used to assign these artificial velocities to interior points; however, such estimates would require a second summation over the particles and, hence, a substantial increase in the computational effort.

This work uses a simpler approach which is stable, accurate, and requires little extra computation. The method is similar to that used by Takeda *et al.* [5] to obtain a functional form for the viscous force due to a solid boundary. Figure 1 illustrates the concept for a portion of a curved boundary. For each fluid particle  $a$ , the normal distance  $d_a$  to the boundary is calculated. This normal is used to define a tangent plane (a line in two dimensions) from which the normal distance  $d_B$  to each boundary particle  $B$  is calculated. The velocity of particle  $a$  is extrapolated across the tangent plane, assuming zero velocity on the plane itself, thus giving each boundary particle velocity  $\mathbf{v}_B = -(d_B/d_a)\mathbf{v}_a$ . In practice, the discrete arrangement of boundary particles may permit a fluid particle to closely approach the nominal curve describing the boundary. In such circumstances, the magnitude of  $\mathbf{v}_B$  must be restricted. Accordingly, the following formula is used to calculate relative velocities between fluid and boundary particles,

$$\mathbf{v}_{ab} = \beta \mathbf{v}_a, \quad (14)$$

where

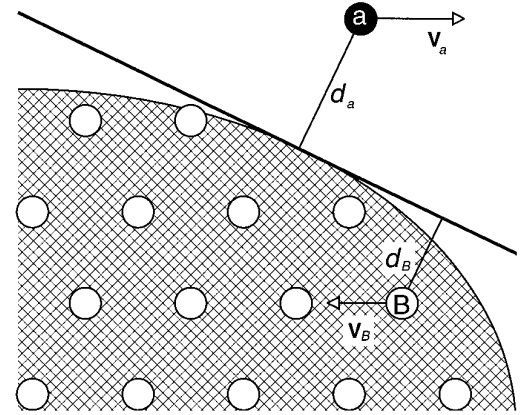


**FIG. 1.** Construction of artificial velocity for boundary particles to simulate a no-slip boundary condition.

$$\beta = \min \left( \beta_{\max}, 1 + \frac{d_B}{d_a} \right). \quad (15)$$

Numerical simulations have shown that good results are obtained if  $\beta_{\max}$  is approximately 1.5. If the boundary is in motion,  $\mathbf{v}_a$  in (14) should be replaced by the fluid velocity relative to the boundary. The artificial velocity  $\mathbf{v}_B$  is used to calculate viscous forces (see Section 2.6)), but it is not used to evolve boundary particle positions. Consequently, the actual boundary velocity is used in (6) such that densities remain consistent with (1). For concave surfaces, a similar method could be used in which the tangent plane is constructed by considering the nearest point on the curve to each boundary particle (rather than fluid particle). The two methods give identical results for a plane surface.

There are alternative techniques which take boundary curvature into account. For example, Monaghan [19, 20] introduced special boundary particle formulations in the context of high Reynolds number free-surface flows which explicitly account for local curvature effects when calculating the contribution from boundary particles. This approach can reduce the noise otherwise introduced by a discrete boundary representation. Similar improvements to the boundary conditions employed here, incorporating approaches taken by other authors for high Reynolds number problems, are the focus of further investigation.

## 2.6. Viscosity

Most implementations of SPH employ an artificial viscosity first introduced to permit the modeling of strong shocks [6, 7]. This viscosity is incorporated into the momentum equation

$$\frac{d\mathbf{v}_a}{dt} = - \sum_b m_b \left( \frac{p_a}{\rho_a^2} + \frac{p_b}{\rho_b^2} + \Pi_{ab} \right) \nabla_a W_{ab}, \quad (16)$$

where

$$\Pi_{ab} = \begin{cases} \frac{-\alpha c \tilde{\mu}_{ab} + \beta \tilde{\mu}_{ab}^2}{\bar{\rho}_{ab}}, & \text{if } \mathbf{v}_{ab} \cdot \mathbf{r}_{ab} < 0; \\ 0, & \text{otherwise,} \end{cases} \quad (17)$$

$$\tilde{\mu}_{ab} = \frac{h \mathbf{v}_{ab} \cdot \mathbf{r}_{ab}}{\mathbf{r}_{ab}^2 + 0.01h^2}, \quad (18)$$

and  $\bar{\rho}_{ab}$  is the average density of particles  $a$  and  $b$ . The  $0.01h^2$  term is included to keep the denominator nonzero. Although this formulation has been used to model real viscosity [4, 22], it produced inaccurate velocity profiles for our simulations. The advantage of (16) is that it guarantees conservation of angular momentum, which is important for applications involving relatively large fluid velocities or an unbounded fluid edge. Since this work involves low velocities and SPH particles fill all space, a more realistic form of viscosity has been adopted. Previous expressions used to calculate realistic viscous forces have typically involved nested summations over the particles [23, 24] (and, hence, twice the computational effort), or have directly employed second derivatives of the kernel [5]. The disadvantage of using second derivatives is that interpolation is much more susceptible to error at low resolution (especially for low-order spline kernels [25]). Our method employs an SPH estimation of viscous diffusion which is similar to an expression used in [26] to model heat conduction,

$$\left\{ \left( \frac{1}{\rho} \nabla \cdot \mu \nabla \right) \mathbf{v} \right\}_a = \sum_b \frac{m_b (\mu_a + \mu_b) \mathbf{r}_{ab} \cdot \nabla_a W_{ab}}{\rho_a \rho_b (\mathbf{r}_{ab}^2 + 0.01h^2)} \mathbf{v}_{ab}, \quad (19)$$

where  $\mu = \rho \nu$  is the dynamic viscosity. This hybrid expression combines a standard SPH first derivative with a finite difference approximation of a first derivative. By taking a Taylor expansion about particle  $a$ , it can be shown that this expression is appropriate [26]. This formulation conserves linear momentum exactly, while angular momentum is only approximately conserved. If the kernel takes the form of (4) then

$$\nabla_a W_{ab} = \frac{\mathbf{r}_{ab}}{|\mathbf{r}_{ab}|} \frac{\partial W_{ab}}{\partial r_a} \quad (20)$$

and we can simplify (19) to

$$\left\{ \left( \frac{1}{\rho} \nabla \cdot \mu \nabla \right) \mathbf{v} \right\}_a = \sum_b \frac{m_b (\mu_a + \mu_b) \mathbf{v}_{ab}}{\rho_a \rho_b} \left( \frac{1}{r_{ab}} \frac{\partial W_{ab}}{\partial r_a} \right). \quad (21)$$

Thus, the momentum equation is written as

$$\begin{aligned} \frac{d\mathbf{v}_a}{dt} = & - \sum_b m_b \left( \frac{p_a}{\rho_a^2} + \frac{p_b}{\rho_b^2} \right) \nabla_a W_{ab} \\ & + \sum_b \frac{m_b (\mu_a + \mu_b) \mathbf{v}_{ab}}{\rho_a \rho_b} \left( \frac{1}{r_{ab}} \frac{\partial W_{ab}}{\partial r_a} \right) + \mathbf{F}_a, \end{aligned} \quad (22)$$

where  $\mathbf{F}_a$  is the body force evaluated at particle  $a$ .

## 2.7. The Kernel

There are many possible choices of the function  $f$  in (4). Most SPH simulations employ a cubic spline kernel [27, 28],

$$f(s) = \frac{10}{7\pi} \begin{cases} 1 - 3s^2/2 + 3s^3/4, & \text{if } 0 \leq s < 1; \\ (2-s)^3/4, & \text{if } 1 \leq s < 2; \\ 0, & \text{if } s \geq 2 \end{cases} \quad (23)$$

(here normalized for two dimensions), since it resembles a Gaussian while having compact support. However, it has been shown that SPH can be unstable to transverse modes when kernels with compact support are used [14, 17, 29]. As higher-order splines more closely approximating a Gaussian are employed, these instabilities are reduced. One reason for the poor performance of lower-order splines is that the stability properties of SPH depend strongly upon the *second* derivative of the kernel. The second derivative of the cubic spline is a piecewise-linear function, and, accordingly, the stability properties are inferior to those of smoother kernels. For example, when the quintic spline [27] is used,

$$f(s) = \frac{7}{478\pi} \begin{cases} (3-s)^5 - 6(2-s)^5 + 15(1-s)^5, & 0 \leq s < 1; \\ (3-s)^5 - 6(2-s)^5, & 1 \leq s < 2; \\ (3-s)^5, & 2 \leq s < 3; \\ 0, & s \geq 3, \end{cases} \quad (24)$$

transverse mode instabilities are negligible [14, 29]. For most applications using a cubic spline, these instabilities are not important since the resulting perturbations in density typically peak at about 1%. However, for a quasi-incompressible equation of state, such variations are significant (see Section 2.3). Thus, for simulations involving very low Reynolds numbers, it was found that a cubic spline rapidly produced significant noise in the pressure and velocity fields, whereas simulations employing the quintic spline remained stable. Although the quintic spline is computationally more intensive (by approximately a factor of 2), it was found to be the most reliable for our simulations.

Morris [29] presents a discussion of alternative kernels which have superior stability properties to standard cubic splines with no extra computational expense. It is not clear, however, if these kernels represent a significant improvement over the quintic spline for a given region of support for this application.

## 2.8. Time Integration

A modified Euler technique was used to perform the time integration. For stability, several time step criteria must be satisfied, including a CFL condition [8],

$$\Delta t \leq 0.25 \frac{h}{c}, \quad (25)$$

and additional constraints due to the magnitude of particle accelerations  $f_a$  [7],

$$\Delta t \leq 0.25 \min_a \left( \frac{h}{f_a} \right)^{1/2}, \quad (26)$$

and viscous diffusion,

$$\Delta t \leq 0.125 \frac{h^2}{\nu}. \quad (27)$$

Equation (27) is based upon the usual condition for an explicit finite difference method simulating diffusion. At sufficiently high resolution (small  $h$ ) or large viscosity, (27) is typically the dominant time constraint. The choice of kernel and the arrangement of particles influences the coefficients in (25)–(27). In particular, different splines can have different “effective” resolution lengths for the same value of  $h$ . For example, use of a cubic spline (which is “narrower” than a quintic for the same smoothing length) may require slightly smaller coefficients in the above expressions.

## 2.9. Summary of the Method

A summary of the method to simulate quasi-incompressible flow at low Reynolds number using SPH can now be presented. The particles are placed on a hexagonal lattice filling all space and assigned a constant initial density ( $\rho_0$ ). Boundary particles are defined as those initially lying inside obstacles within the flow field and beyond solid walls. The equation of state for the fluid is given by (10) and the sound speed  $c$  is chosen such that density fluctuations are at most 3%. In the case of periodic flow driven by an applied pressure gradient, the dynamic pressure (7) is used and the applied pressure differential is simulated by an applied body force (8). For stability at low Reynolds numbers, a quintic spline kernel is used with a smoothing length of 1.5 times the initial nearest neighbor distance. Particle densities are evolved using (6) to reduce the computational effort, and the particle

velocities are evolved according to (22). To ensure stability of the integration scheme, the time step is limited according to the conditions set forth in Section 2.8. No-slip boundary conditions are simulated by assigning artificial velocities to the boundary particles using (14).

## 3. MODEL TESTING AND VERIFICATION

### 3.1. Couette Flow

The first test case is Couette flow between infinite plates located at  $y = 0$  and  $y = L$ . The system is initially at rest. At time  $t = 0$ , the upper plate moves at constant velocity  $V_0$  parallel to the  $x$ -axis. The series solution for the time-dependent behavior of this flow is

$$v_x(y, t) = \frac{V_0}{L} y + \sum_{n=1}^{\infty} \frac{2V_0}{n\pi} (-1)^n \sin\left(\frac{n\pi}{L} y\right) \exp\left(-\nu \frac{n^2\pi^2}{L^2} t\right), \quad (28)$$

where  $v_x$  is the fluid velocity in the  $x$ -direction. The flow was simulated using SPH for  $\nu = 10^{-6}\text{m}^2\text{s}^{-1}$ ,  $L = 10^{-3}\text{m}$ ,  $\rho = 10^3\text{kkgm}^{-3}$ ,  $V_0 = 1.25 \times 10^{-5}\text{ms}^{-1}$ , and with 50 particles spanning the channel. This corresponds to a Reynolds number of  $1.25 \times 10^{-2}$ , using

$$\text{Re} = \frac{V_0 L}{\nu}. \quad (29)$$

Figure 2 shows a comparison between velocity profiles obtained using (28) and SPH at several times including the steady state solution ( $t = \infty$ ). The results are in close agreement (within 0.5%), confirming the accuracy of the approach used to evaluate viscous and boundary forces with SPH. Lower resolution simulations completed with 20 particles spanning the channel were found to agree to within approximately 2% of the series solution values.

### 3.2. Poiseuille Flow

The second test case is Poiseuille flow between stationary infinite plates at  $y = 0$  and  $y = L$ . The fluid is initially at rest and is driven by an applied body force  $F$  parallel to the  $x$ -axis for  $t \geq 0$ . The series solution for the transient behavior is

$$v_x(y, t) = \frac{F}{2\nu} y(y - L) + \sum_{n=0}^{\infty} \frac{4FL^2}{\nu\pi^3(2n+1)^3} \sin\left(\frac{\pi y}{L}(2n+1)\right) \exp\left(-\frac{(2n+1)^2\pi^2\nu}{L^2} t\right). \quad (30)$$

SPH was used to simulate Poiseuille flow for  $\nu = 10^{-6}\text{m}^2\text{s}^{-1}$ ,  $L = 10^{-3}\text{m}$ ,  $\rho = 10^3\text{kkgm}^{-3}$ ,  $F = 10^{-4}\text{ms}^{-2}$ , and 50 particles

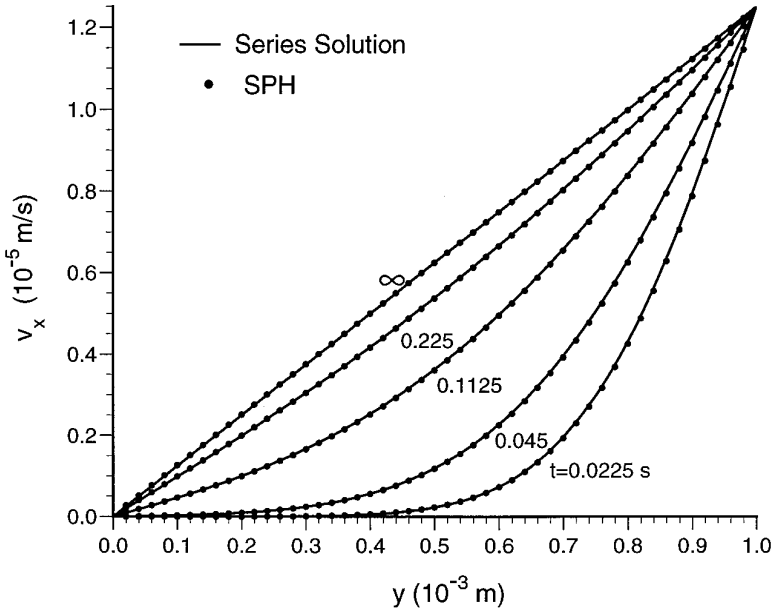


**FIG. 2.** Comparison of SPH and series solutions for Couette flow ( $\text{Re} = 1.25 \times 10^{-2}$ ).

spanning the channel. This corresponds to a peak fluid velocity  $V_0 = 1.25 \times 10^{-5} \text{ ms}^{-1}$  and a Reynolds number of  $1.25 \times 10^{-2}$  using (29). A comparison between velocity profiles obtained using (30) and SPH appears in Fig. 3. The results are again in close agreement, with the largest discrepancy being about 0.7% for the steady state solution. Lower resolution simulations completed with 20 particles

spanning the channel agreed to within approximately 2% of the series solution values.

### 3.3. Flow through a Periodic Lattice of Cylinders

The Couette and Poiseuille simulations tested the interaction between viscous and body forces and the effective-

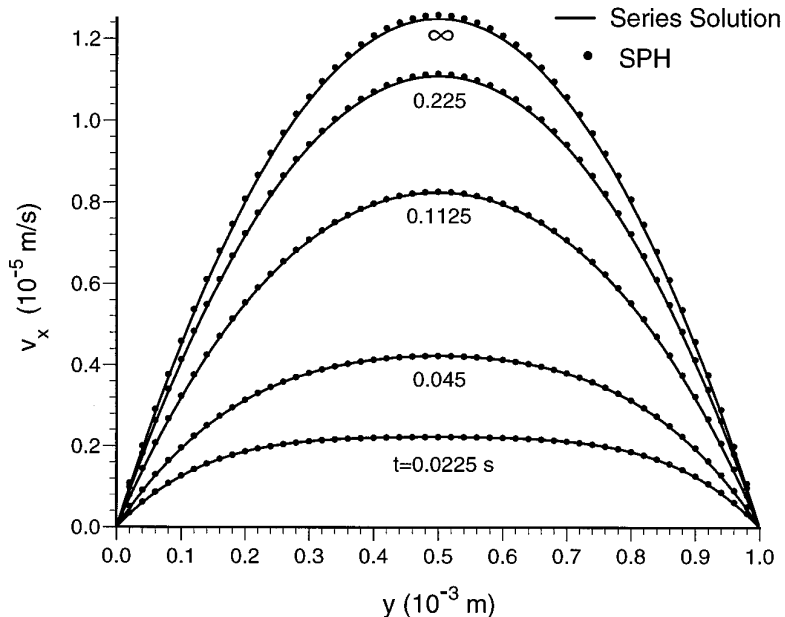


**FIG. 3.** Comparison of SPH and series solutions for Poiseuille flow ( $\text{Re} = 1.25 \times 10^{-2}$ ).

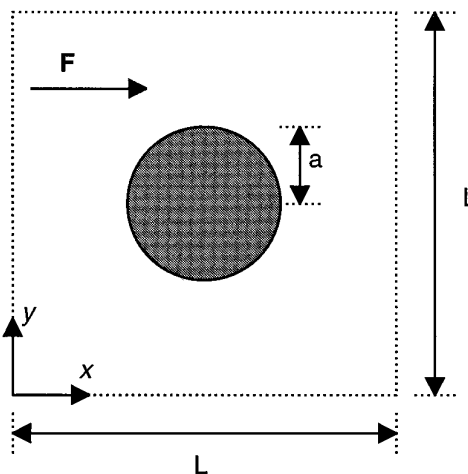
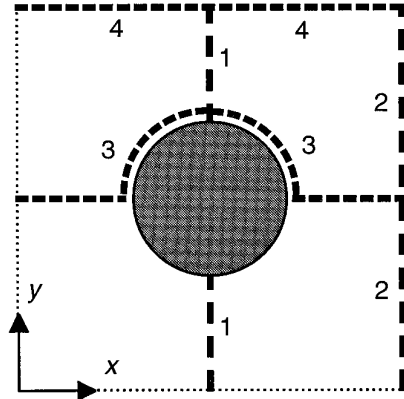


**FIG. 4.** Single cylinder within a periodic lattice.

ness of the no-slip boundary condition in the SPH model. However, these flows are one dimensional and do not produce variations in dynamic pressure. A more challenging test of the method involves flow through a square lattice of cylinders. This particular configuration has been studied extensively [30–32] as a simple model of flow through fibrous porous media. To solve this problem with SPH, a single cylinder and its associated volume within the lattice is considered (Fig. 4). Flow is driven by a pressure gradient (modeled using an effective body force  $F$ ), and periodic boundary conditions are applied to model an infinite periodic array.

### 3.3.1. Low Reynolds Number

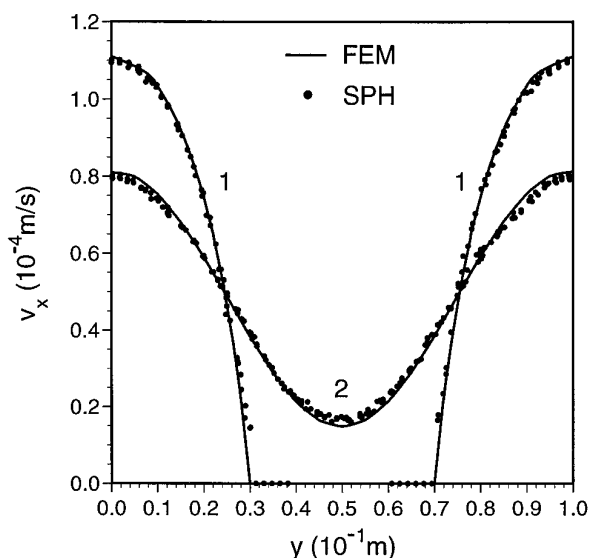
Periodic flow past a cylinder was simulated using SPH for  $L = 0.1$  m,  $\nu = 10^{-6}$  m $^2$ s $^{-1}$ ,  $a = 2 \times 10^{-2}$  m,  $F = 1.5 \times 10^{-7}$  ms $^{-2}$ , and  $c = 5.77 \times 10^{-4}$  ms $^{-1}$ . Replacing  $L$  with  $a$  in (29) and taking the velocity scale to be  $V_0 = 5 \times 10^{-5}$  ms $^{-1}$  gives  $Re = 1$ . The SPH simulation was run using approximately 3000 particles placed on a hexagonal lattice with a nearest neighbor distance of 0.002 m. The cylinder was modeled by considering all particles within its perimeter to be of the type described in Section 2.5. The particles started from rest and steady state was reached after approximately 1500 steps. To investigate long-term behavior, the simulation was continued for another 6000 steps such that particle arrangements became disordered. The problem was also modeled using a finite element method (FEM) program for steady incompressible viscous flow. Velocity and pressure distributions from the two solutions were compared by plotting values within one nearest neighbor distance of the four paths described in Fig. 5. The results were also compared using contour plots. As the FEM employs a mesh to obtain a solution, it is relatively easy to obtain contour plots. The corresponding plots for SPH



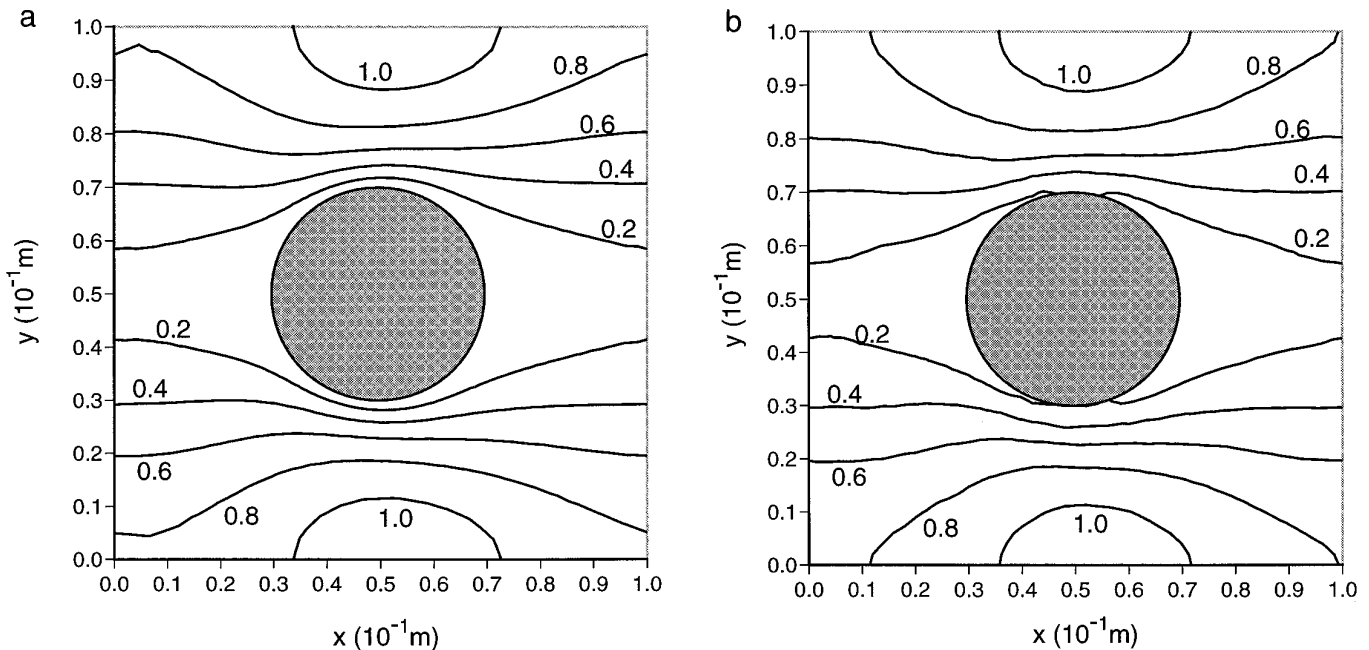
**FIG. 5.** Paths for comparison of SPH and FEM solutions.

were obtained by interpolating the particle quantities to a 50 by 50 array of grid points using the quintic kernel. Smoothing lengths of 1 and 3 grid spacings were used for the velocity and pressure, respectively. A greater amount of smoothing was needed to remove small fluctuations from the pressure field. Contours generated using this method are inaccurate in the immediate vicinity of the cylinder.

Figure 6 shows a comparison of velocity profiles obtained using SPH and FEM for paths 1 and 2 defined in Fig. 5. The results obtained using SPH are in close agreement with those from the FEM throughout the flow domain. Corresponding contour plots of velocity magnitude are shown in Fig. 7. Good agreement is obtained for the bulk of the flow, although the contour smoothing method inaccurately represents SPH velocities near the cylinder.



**FIG. 6.** Comparison of SPH and FEM velocity profiles along paths 1 and 2 for  $Re = 1$ .



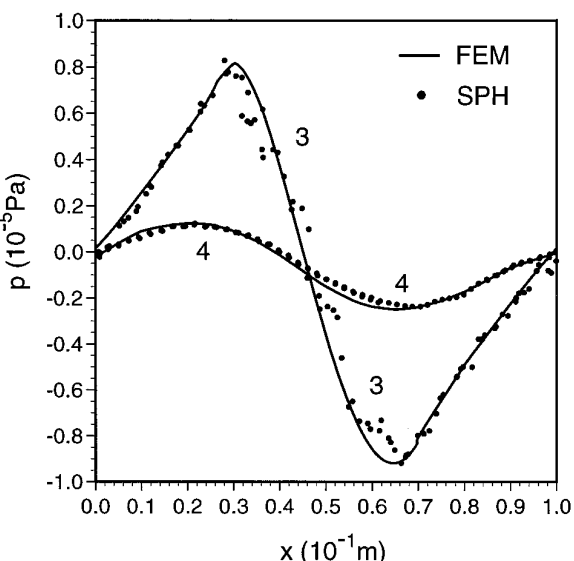
**FIG. 7.** Contour plots of velocity magnitude using (a) FEM and (b) SPH for  $\text{Re} = 1$  (contour lines are labeled in units of  $10^{-4}\text{m/s}$ ).

Figure 8 shows the dynamic pressure along paths 3 and 4 (Fig. 5). The arc of path 3 was taken 0.002 m (one SPH nearest neighbor distance) beyond the cylinder boundary since the SPH boundary particles may not necessarily lie on the boundary surface itself. The SPH dynamic pressure profile shows small local fluctuations in the vicinity of the cylinder. Elsewhere, the SPH and

FEM solutions are in close agreement. The peaks in the pressure obtained using SPH on the boundary itself fell short of the FEM results by approximately 8%. The FEM better captures pressure extrema since grid-stretching increases resolution in the vicinity of the cylinder. Corresponding contour plots of pressure given in Fig. 9 show that good agreement is again obtained for the bulk of the flow. This simulation was repeated with twice the particle resolution (approximately 11,000 particles) and peak pressures were reproduced to within 5%. Pressure values in the immediate vicinity of the boundary, however, still exhibited small fluctuations.

### 3.3.2. Very Low Reynolds Number

Flow through a periodic lattice of cylinders was also solved for  $L = 0.1 \text{ m}$ ,  $\nu = 10^{-4}\text{m}^2\text{s}^{-1}$ ,  $a = 2 \times 10^{-2}\text{m}$ ,  $F = 5 \times 10^{-5}\text{ms}^{-2}$ , and  $c = 1 \times 10^{-2}\text{ms}^{-1}$ . Taking  $V_0 = 1.5 \times 10^{-4}\text{ms}^{-1}$ , this gives  $\text{Re} = 0.03$ . Once again, the simulation was initialized with zero velocity and the steady state was reached after approximately 1500 steps. However, the initial lattice was relatively unchanged at this point. To demonstrate the long-term behavior of the method, the simulation was run for another 300,000 steps. The final particle configuration, shown in Fig. 10, was typical of those observed in these simulations once the initial lattice had broken up. A comparison of velocities along paths 1 and 2 appears in Fig. 11 and velocity contour plots are shown in Fig. 12. The results obtained using SPH are in close agreement with those obtained by the FEM. The flux



**FIG. 8.** Comparison of SPH and FEM pressure profiles along paths 3 and 4 for  $\text{Re} = 1$ .

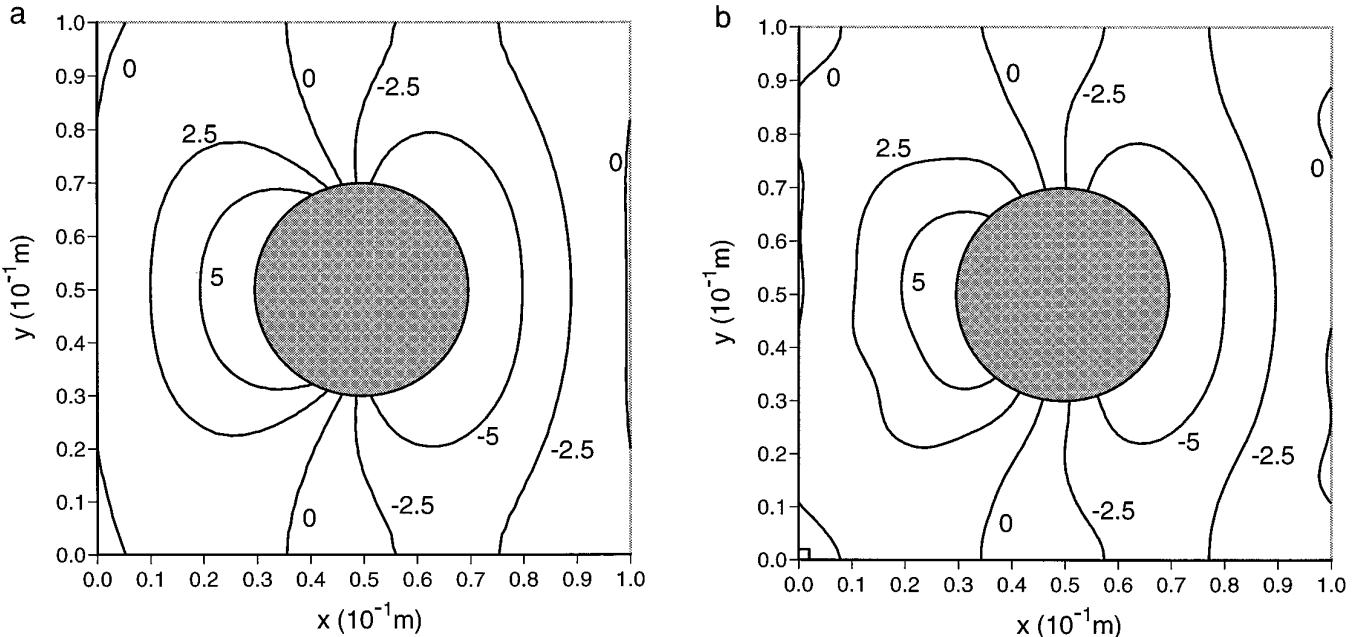


**FIG. 9.** Contour plots of pressure using (a) FEM and (b) SPH for  $Re = 1$  (contour lines are labeled in units of  $10^{-6}$  Pa).

through the lattice is  $1.70 \times 10^{-4}$  m/s, which agrees to within 3% with the analytical solution of Drummond and Tahir [31] for Stokes flow. A comparison of pressure fields presented in Figs. 13 and 14 also shows close agreement for the bulk of the flow, with similar fluctuations as observed for  $Re = 1$ . Although pressure extrema on the boundary

were not fully captured by SPH, the discrepancies were somewhat smaller (about 5%). The simulation was repeated for fewer time steps with twice the resolution (approximately 11,000 particles) and peak pressures were obtained with less than 4% error. Once again, however, small pressure fluctuations were observed near the boundary.

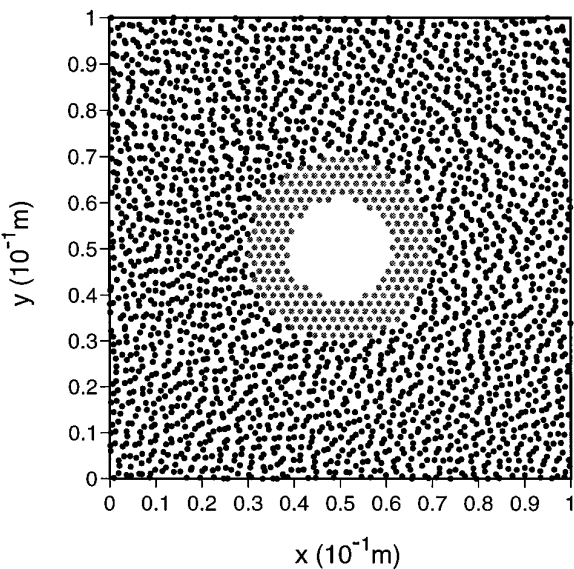


**FIG. 10.** Final particle positions corresponding to the results presented for  $Re = 0.03$ . Fluid and boundary particles are shown in black and gray, respectively.

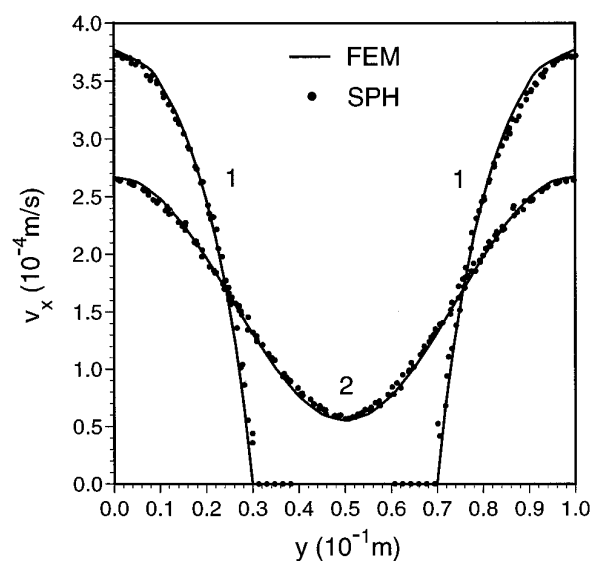


**FIG. 11.** Comparison of SPH and FEM velocity profiles along paths 1 and 2 for  $Re = 0.03$ .

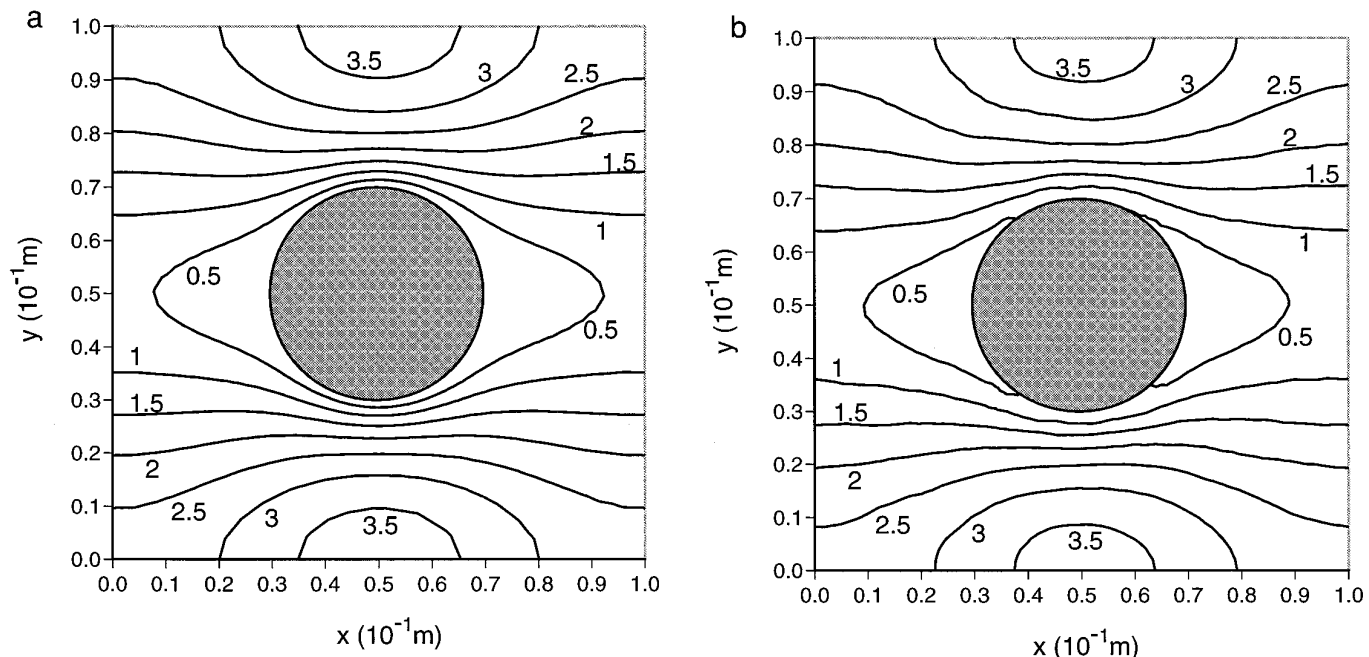


**FIG. 12.** Contour plots of velocity magnitude using (a) FEM and (b) SPH for  $Re = 0.03$  (contour lines are labeled in units of  $10^{-4}$  m/s).

#### 4. CONCLUSIONS AND FUTURE WORK

Extensions of the method of smoothed particle hydrodynamics (SPH) have been presented which allow the simulation of incompressible flows for low Reynolds numbers. Results suggest that the proposed equation of state, viscosity formulation, boundary conditions, and interpolation

kernel result in a method which is stable and gives accurate estimates of velocity for problems of the type considered. Peak pressures on solid boundaries are smoothed out at lower resolutions, but are achieved to within 5% for simulations involving over 10,000 particles. However, pressures in the vicinity of a circular boundary exhibited local fluctuations of several percent. Further improvements to the boundary conditions may be possible which will reduce these errors (see Section 2.5). Additional tests involving convex and concave boundary surfaces are planned.

Straightforward extensions of the method are possible which will increase its utility. For example, it is possible to simulate the dispersion of a solute through the lattice of cylinders described in Section 3.3. A quantity which does not influence the flow (e.g., the concentration of a dilute solute) may be evolved independently from one cell to the next while still assuming the velocity and density fields are periodic. As most of the computational expense is associated with locating and summing over nearest neighbors, the increase in work is moderate. A method similar to that used here may permit the simulation of other flows at low Reynolds numbers using SPH. However, further development will be needed for cases involving free surfaces or substantially different equations of state. The extension to three-dimensional problems is, in theory, straightforward. Obtaining steady-state results is relatively inexpensive, however, extended simulations in three-dimensions involving many crossing times at very low Reynolds numbers will probably necessitate the use of

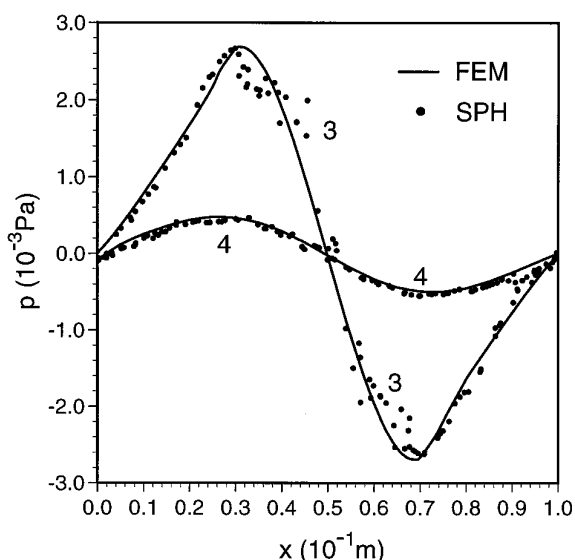


**FIG. 13.** Comparison of SPH and FEM pressure profiles along paths 3 and 4 for  $Re = 0.03$ .

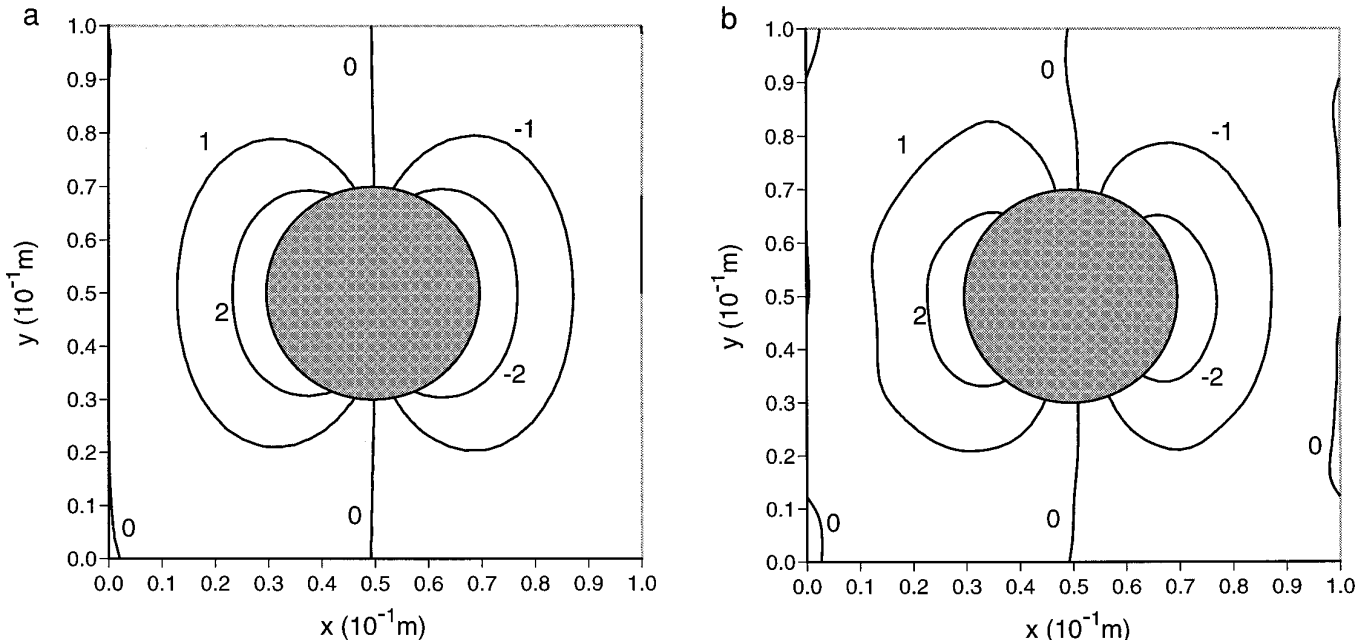


**FIG. 14.** Contour plots of pressure using (a) FEM and (b) SPH for  $\text{Re} = 0.03$  (contour lines are labeled in units of  $10^{-3} \text{Pa}$ ).

supercomputers. A modification of the method to include surface tension is currently being undertaken to simulate the flow of multiphase fluids in porous media.

#### ACKNOWLEDGMENT/DISCLAIMER

This work was sponsored by the Air Force Office of Scientific Research, USAF, under Grant F49620-96-1-0020. The views and conclusions contained herein are those of the authors and should not be interpreted as necessarily representing the official policies or endorsements, either expressed or implied, of the Air Force Office of Scientific Research or the U.S. Government.

#### REFERENCES

1. L. B. Lucy, A numerical approach to the testing of the fission hypothesis, *Astron. J.* **83**, 1013 (1977).
2. R. A. Gingold and J. J. Monaghan, Smoothed particle hydrodynamics: Theory and application to non-spherical stars, *Mon. Not. R. Astron. Soc.* **181**, 375 (1977).
3. J. J. Monaghan, Simulating free surface flows with SPH, *J. Comput. Phys.* **110**, 399, (1994).
4. P. Artynowicz and S. H. Lubow, Dynamics of binary-disk interaction. 1. Resonances and disk gap sizes, *Astrophys. J.* **421**, 651 (1994).
5. H. Takeda, S. M. Miyama and M. Sekiya, Numerical simulation of viscous flow by Smoothed Particle Hydrodynamics, *Prog. Theor. Phys.* **92**(5), 939 (1994).
6. W. Benz, Smooth particle hydrodynamics: A review, in *NATO Workshop, Les Arcs, France, 1989*.
7. J. J. Monaghan, Smoothed Particle Hydrodynamics, *Annu. Rev. Astron. Astrophys.* **30**, 543 (1992).
8. R. Courant, K. Friedrichs, and H. Lewy, Über die partiellen differen-
- zengleichungen der mathematischen physik, *Math. Ann.* **100**, 32 (1928).
9. A. J. Chorin, A numerical method for solving incompressible flow problems, *J. Comput. Phys.* **2**, 12 (1967).
10. E. Turkel, Preconditioned methods for solving the incompressible and low-speed compressible equations, *J. Comput. Phys.* **72**, 277 (1987).
11. P. Tamamidis, G. Zhang, and D. N. Assanis, Comparison of pressure-based and artificial compressibility methods for solving three-dimensional steady incompressible viscous flows, *J. Comput. Phys.* **124**, 1 (1996).
12. J. J., Monaghan, Simulating gravity currents with SPH lock gates, *Applied Mathematics Reports and Preprints 95/5*, Monash University, 1995. (unpublished)
13. G. K. Batchelor, *An Introduction to Fluid Dynamics*. (Cambridge Univ. Press, Cambridge, UK, 1967).
14. J. P. Morris, A study of the stability properties of SPH, *Applied Mathematics Reports and Preprints 94/22*, Monash University, Melbourne, Australia, 1994. (unpublished)
15. D. S. Balsara, Von-Neumann stability analysis of Smoothed Particle Hydrodynamics: Suggestions for optimal algorithms, *J. Comput. Phys.* **121**, 357 (1995).
16. J. W. Swegle, D. L. Hicks and S. W. Attaway, Smoothed Particle Hydrodynamics stability analysis, *J. Comput. Phys.* **116**, 123 (1995).
17. J. P. Morris, Stability Properties of SPH, *Publ. Astron. Soc. Aust.* **13**, 97 (1996).
18. J. J. Monaghan, On the problem of penetration in particle methods, *J. Comput. Phys.* **82**, 1 (1989).
19. J. J. Monaghan, Improved modelling of boundaries, *Applied Mathematics Reports and Preprints 95/30*, Monash University, Melbourne, Australia, 1995. (unpublished)
20. J. J. Monaghan, Simulating gravity currents with SPH: III boundary forces, *Applied Mathematics Reports and Preprints 95/11*, Monash University, Melbourne, Australia, 1995. (unpublished)

21. L. D. Libersky, A. G. Petschek, T. C. Carney, J. R. Hipp, and F. A. Allahdadi, High strain Lagrangian hydrodynamics, *J. Comput. Phys.* **109**, 67 (1993).
22. S. T. Maddison, J. R. Murray, and J. J. Monaghan, SPH simulations of accretion disks and narrow rings, *Publ. Astron. Soc. Aust.* **13**, 66 (1996).
23. O. Flebbe, S. Münzel, H. Herold, H. Riffert, and H. Ruder, Smoothed Particle Hydrodynamics: Physical viscosity and the simulation of accretion disks, *Astrophys. J.* **431**, 754 (1994).
24. S. J. Watkins, A. S. Bhattacharjee, N. Francis, J. A. Turner, and A. P. Whitworth, A new prescription for viscosity in Smoothed Particle Hydrodynamics, *Astron. Astrophys. Suppl. Ser.* **119**, 177 (1996).
25. L. Brookshaw, A method of calculating radiative heat diffusion in particle simulations, *Proc. Astron. Soc. Aust.* **6**, 207, (1985).
26. J. J. Monaghan, Heat conduction with discontinuous conductivity, Applied Mathematics Reports and Preprints **95/18**, Monash University, Melbourne, Australia, 1995. (unpublished)
27. Schoenberg, I. J., Contributions to the problem of approximation of equidistant data by analytic functions, *Q. Appl. Math.* **4**, 45 (1946).
28. Monaghan, J. J. and Lattanzio, J. C., A refined particle method for astrophysical problems, *Astron. Astrophys.* **149**, 135 (1985).
29. J. P. Morris, *Analysis of Smoothed Particle Hydrodynamics with Applications*, Ph.D. thesis, Monash University, Melbourne, Australia, 1996.
30. N. Epstein and J. H. Masliyah, Creeping flow through clusters of spheroids and elliptical cylinders, *Chem. Engr. J.* **3**, 169 (1972).
31. J. E. Drummond and M. I. Tahir, Laminar viscous flow through regular arrays of parallel solid cylinders, *Int. J. Multiphase Flow* **10**, 515 (1984).
32. G. W. Jackson and D. F. James, The permeability of fibrous porous media, *Can. J. Chem. Eng.* **64**, 364 (1986).